Supplementary Text
Hidden liquid-crystalline order in a non-collinear antiferromagnet

Shashank Kumar Ojha[1,2] *†, Sergei Prokhorenko[3] ‡, Maya Ramesh[4] §, Xinyan Li[1,2], Richa Mudgal[1,2], Nicholas Reiterer[5] Akash Surampalli[1,2], Surya Narayan Panda[1,2], Pushpendra Gupta[5], Yousra Nahas[3], Yimo Han[1,2], Paul Stevenson[6], Lane W. Martin[1,2,7,8], Laurent Bellaiche[3,9], Darrell G. Schlom[3,10,11], Sajid Husain[5,12]¶, Ramamoorthy Ramesh[1,5,12,13]‖

June 28, 2026

[1]Department of Materials Science and NanoEngineering, Rice University, Houston, TX, USA
[2]Rice Advanced Materials Institute, Rice University, Houston, TX, USA
[4]Department of Materials Science and Engineering, Cornell University, Ithaca, USA
[3]Smart Ferroic Materials Center, Physics Department and Institute for Nanoscience and Engineering, University of Arkansas, Fayetteville, Arkansas 72701, USA
[5]Department of Materials Science and Engineering, University of California, Berkeley, CA, USA
[6]Department of Physics, Northeastern University, Boston, MA 02115, USA
[7]Department of Physics and Astronomy, Rice University, Houston, TX, USA
[8]Department of Chemistry, Rice University, Houston, TX, USA
[9]Department of Materials Science and Engineering, Tel Aviv University, Ramat Aviv, Tel Aviv 6997801, Israel
[10]Kavli Institute at Cornell for Nanoscale Science, Cornell University, Ithaca, NY, 14853, USA
[11]Leibniz-Institut fur Kristallzüchtung, Max-Born-Str. 2, 12489, Berlin, Germany
[12]Department of Physics, University of California, Berkeley, CA, USA
[13]Materials Science Division, Lawrence Berkeley National Laboratory, Berkeley, CA, USA

*Corresponding author. Email: so37@rice.edu
†Equal contribution
‡Equal contribution
§Equal contribution
¶Corresponding author. Email: shusain@berkeley.edu
‖Corresponding author. Email: rramesh@berkeley.edu

Supplementary Note 1

Cycloid elastic coefficients

In this section, we derive the cycloid stiffness coefficients starting from the classical lattice Hamiltonian

$$H = -\frac{1}{2}\sum_{ij} J_{ij}^{\alpha\beta} s_i^{\alpha} s_j^{\beta} + \frac{1}{2}\sum_{ij} \mathbf{D}_{ij}[\mathbf{s}_i \times \mathbf{s}_j] + K\sum_i (\mathbf{s}_i \mathbf{e}_P)^2, \tag{1}$$

where J, D, and K constants characterize symmetric super exchange, anti-symmetric Dzyaloshinskii-Moriya vector and the single ion magnetic anisotropy, respectively. The ij sum double counts the bonds with $1/2$ factor restoring it to a pair sum. The positive/negative J_{ij} values correspond to FM/AFM coupling and the unit-length vector along the ferroelectric polarization direction is denoted as $\mathbf{e}_P$. We further assume a modulated G-AFM state Ansatz describing the lattice spins orientation vectors $\mathbf{s}_i$

$$\mathbf{s}_i = e^{i\mathbf{Q}\mathbf{r}_i}\sqrt{1-\mathbf{m}_i^2}\,\mathbf{n}_i + \mathbf{m}_i \tag{2}$$

where $\mathbf{Q} = \frac{\pi}{a_0}(0.5, 0.5, 0.5)$ is the wave-vector characterizing the modulation of G-AFM state at the R point of the pseudo-cubic BZ and a_0 denotes the lattice constant. Explicitly separating the AFM modulation allows us to introduce the normalized Néel vector $\mathbf{n}_i$ and the dimensionless weak magnetization $\mathbf{m}_i$. To simplify the notation, we further introduce $\eta_i = e^{i\mathbf{Q}\mathbf{r}_i}$ and $\gamma_i = \sqrt{1-\mathbf{m}_i^2}$. Substituting the corresponding scalars into Eq.(2), we obtain

$$\mathbf{s}_i = \eta_i\gamma_i\,\mathbf{n}_i + \mathbf{m}_i. \tag{3}$$

Since both $\mathbf{n}_i$ and $\mathbf{m}_i$ are "slow" variables characterizing the cycloidal modulation of the G-AFM state, it is natural to evaluate Eq.(1) in the continuum limit. The corresponding energy density functional $E[\mathbf{n}, \mathbf{m}]$ is obtained by replacing lattice sums with integrals $\sum_i \to 1/a_0^3 \int d^3r$ and expanding $\mathbf{n}_j = \mathbf{n}(\mathbf{r}_j)$ as well as $\mathbf{m}_j = \mathbf{m}(\mathbf{r}_j)$ in powers of the lattice derivative $D = \boldsymbol{\tau}_{ij}\cdot\boldsymbol{\nabla}$. In the latter expression, $\boldsymbol{\tau}_{ij}$ denotes the bond vector connecting nearest neighbor lattice sites. After some algebra and simplifications described in subsection "Auxiliary expressions", we obtain

$$\begin{aligned} E[\mathbf{n},\mathbf{m}] = &- A + \mathcal{J}_1\|\boldsymbol{\nabla}\mathbf{n}\|_F^2 + 3\mathcal{J}_2|(\mathbf{e_P}\cdot\nabla)\,\mathbf{n}|^2 + \Lambda\,\mathbf{m}^2 + \mathcal{K}(\mathbf{n}\cdot\mathbf{e}_P)^2 + \\ &+ \mathcal{D}_w\,\mathbf{e}_P\cdot[\mathbf{n}\times\mathbf{m}] - \mathcal{D}_{sc}\,[\mathbf{e_P}\cdot(\mathbf{n}\cdot\boldsymbol{\nabla})\mathbf{n} - (\mathbf{n}\cdot\mathbf{e}_P)(\boldsymbol{\nabla}\cdot\mathbf{n})]\,, \end{aligned} \tag{4}$$

where $\|\boldsymbol{\nabla}\mathbf{n}\|_F^2 = \sum_{\alpha,\gamma}(\partial_\gamma n_\alpha)^2$ denotes the Frobenius norm and the correspondence between the coefficients in Eq.(4) and the parameters of the microscopic Hamiltonian Eq.(1) are given in Table 1.

The energy functional given by Eq.(4) that we have derived from the lattice Hamiltonian Eq. (1) is consistent with the commonly used continuum functional for $BiFeO_3$ but has an additional anisotropy term consistent with the $R3c$ space group symmetry - an anisotropic exchange stiffness described by the $\mathcal{J}_2$ coefficient that arises from the second nearest neighbor lattice exchange. For the G-AFM cycloid ground state, this $\mathcal{J}_2$ term renormalizes the exchange stiffness along the rhombohedral $\mathbf{e_P}$ axis. Additionally, we note that the terms determining the cycloid propagation direction within the $\mathbf{e_P}$ plane are of higher order in the derivatives $a_0\nabla$.

Starting from Eq.(4) we now derive the elastic Frank-like coefficients for the G-AFM cycloid state. For this, we impose a perturbed cycloid state Ansatz

$$\mathbf{n} = \mathbf{e}_z(\mathbf{r})\cos\theta + \chi\,\mathbf{e}_\mathbf{q}(\mathbf{r})\sin\theta, \tag{5}$$

where $\chi = \pm 1$ defines the sense of the cycloid rotation and the local spin rotation frame is defined by the unit vector $\mathbf{e}_z$ and the cycloid wave-vector direction $\mathbf{q}$ direction $\mathbf{e}_\mathbf{q}$. Both $\mathbf{e}_z$ are allowed to change in space, but are subject to constraint $\mathbf{e}_z \perp \mathbf{e}_\mathbf{q}$ which guarantees proper normalization of the adopted Ansatz Eq.(5). Furthermore, we assume that the phase θ can be expressed as $\theta = \mathbf{q}\cdot\mathbf{r}$. Thereby, the phase normal $\nabla\theta$ remains orthogonal to $\mathbf{e}_z$ which explicitly prohibits Frank twists.

Substituting Eq.(5) into the exchange $\mathcal{J}_1$ contribution from Eq.(4) and averaging over a single phase θ period $\langle \dots \rangle_\theta$, we obtain

$$\left\langle \|\nabla\mathbf{n}\|_F^2 \right\rangle_\theta = q^2 + \frac{1}{2}\|\nabla\mathbf{e}_z\|_F^2 + \frac{1}{2}\|\nabla\mathbf{e}_\mathbf{q}\|_F^2 + 2q\,\chi\,\mathbf{e}_\mathbf{q}\cdot[(\mathbf{e}_\mathbf{q}\cdot\nabla)\,\mathbf{e}_z], \tag{6}$$

while the $\mathcal{J}_2$ contribution results in

$$\left\langle |(\mathbf{e}_\mathbf{P}\cdot\nabla)\,\mathbf{n}|^2 \right\rangle_\theta = q^2(\mathbf{e}_\mathbf{q}\cdot\mathbf{e}_\mathbf{P})^2 + \frac{1}{2}(|\partial_P\,\mathbf{e}_z|^2 + |\partial_P\,\mathbf{e}_\mathbf{q}|^2) + 2\chi q\,(\mathbf{e}_\mathbf{q}\cdot\mathbf{e}_\mathbf{P})(\mathbf{e}_\mathbf{q}\cdot\partial_P\,\mathbf{e}_z), \tag{7}$$

where $\partial_P = \mathbf{e}_\mathbf{P}\cdot\boldsymbol{\nabla}$ denotes the derivative along the polar axis $\mathbf{e}_\mathbf{P}$ direction.

Similar calculations for the Lifshitz invariant give

$$\begin{aligned}\left\langle\, \mathbf{e}_\mathbf{P}\cdot(\mathbf{n}\cdot\boldsymbol{\nabla})\mathbf{n} - (\mathbf{n}\cdot\mathbf{e}_\mathbf{P})(\boldsymbol{\nabla}\cdot\mathbf{n})\right\rangle_\theta = -\chi\,(\mathbf{e}_\mathbf{P}\cdot\mathbf{e}_z)q - \frac{1}{2}\left[(\mathbf{e}_\mathbf{P}\cdot\mathbf{e}_z)(\boldsymbol{\nabla}\cdot\mathbf{e}_\mathbf{z}) + (\mathbf{e}_\mathbf{P}\cdot\mathbf{e}_q)(\boldsymbol{\nabla}\cdot\mathbf{e}_q)\right] + \\ + \frac{1}{2}\mathbf{e}_\mathbf{P}\cdot\left[(\mathbf{e}_z\cdot\boldsymbol{\nabla})\mathbf{e}_z + (\mathbf{e}_q\cdot\boldsymbol{\nabla})\mathbf{e}_q\right].\end{aligned} \tag{8}$$

The energy density contributions related to the weak magnetization in Eq. (4) results only in renormalization of the anisotropy constant $\mathcal{K}$, which is an order of magnitude smaller compared to other energy contributions and will be neglected here. Gathering the derived Eqs.(6-8) we obtain an effective deformation potential

$$\begin{aligned}F_\theta = \mathcal{J}_1\left[q^2 + \frac{1}{2}\|\boldsymbol{\nabla}\mathbf{e}_z\|_F^2 + \frac{1}{2}\|\boldsymbol{\nabla}\mathbf{e}_q\|_F^2 + 2q\,\chi\,\mathbf{e}_\mathbf{q}\cdot[(\mathbf{e}_q\cdot\boldsymbol{\nabla})\mathbf{e}_z]\right] + \\ + 3\mathcal{J}_2\left[q^2\,(\mathbf{e}_\mathbf{q}\cdot\mathbf{e}_\mathbf{P})^2 + \frac{1}{2}(|\partial_P\,\mathbf{e}_z|^2 + |\partial_P\,\mathbf{e}_\mathbf{q}|^2) + 2\chi q\,(\mathbf{e}_\mathbf{q}\cdot\mathbf{e}_\mathbf{P})(\mathbf{e}_\mathbf{q}\cdot\partial_P\,\mathbf{e}_z)\right] + \\ + \mathcal{D}_{sc}\left[\chi(\mathbf{e}_P\cdot\mathbf{e}_z)q + \frac{1}{2}\left((\mathbf{e}_P\cdot\mathbf{e}_z)\,(\boldsymbol{\nabla}\cdot\mathbf{e}_z) + (\mathbf{e}_P\cdot\mathbf{e}_q)\,(\boldsymbol{\nabla}\cdot\mathbf{e}_q)\right)\right. \\ \left. -\frac{1}{2}\mathbf{e}_P\cdot((\mathbf{e}_z\cdot\boldsymbol{\nabla})\mathbf{e}_z + (\mathbf{e}_q\cdot\boldsymbol{\nabla})\mathbf{e}_q)\right],\end{aligned} \tag{9}$$

Eq. (9) can serve as a basis for mapping of the cycloidal deformation energy to the corresponding potential of liquid crystal state. Particularly, the square of Frobenius norms of the $\boldsymbol{\nabla}\mathbf{e}_z$ and $\boldsymbol{\nabla}\mathbf{e}_q$

matrices represent the isotropic energy cost of bending/splay and twist. Other terms, also have a geometric meaning and serve as anisotropic constraints. Particularly, the $\mathcal{J}_2$ contributions distinguish between deformations constrained to the plane perpendicular to the polarization direction $\mathbf{e_P}$ and deformations that make the propagation vector direction $\mathbf{e_q}$ bend or twist away from such plane. To make the analogy between the $BiFeO_3$ cycloid states and liquid crystals more explicit, we now proceed by analyzing some particular cases of Eq.(9). To simplify the analysis, we will constrain ourselves to the ferroelectric monodomain state characterized by the $\mathbf{e_P} = \text{const}$ conditions.

For this, we set ($\mathbf{e}_P = \frac{1}{\sqrt{3}}[1,1,1]_{\text{p.c.}}$). A pure compression/elongation corresponds to

$$\partial_\alpha e_q^\gamma = \partial_\alpha e_P^\gamma = 0, \ \forall \alpha, \gamma$$

deformation which further simplifies Eq.(9) to

$$F_\theta = \left[\mathcal{J}_1 + 3\mathcal{J}_2 \left(\mathbf{e_q} \cdot \mathbf{e_P}\right)^2\right] q^2 + \chi D_{sc} \left(\mathbf{e_P} \cdot \mathbf{e_z}\right) q. \tag{10}$$

For $\mathcal{J}_2 > 0$, the ground state is the standard cycloid solution with $\mathbf{e_q} \perp \mathbf{e_P}$, $\mathbf{e}_z \parallel \mathbf{e_P}$. An equilibrium wave-vector amplitude q_0 is then equal to

$$q_0 = \frac{D_{sc}}{2\mathcal{J}_1},$$

so that the energy can be rewritten as

$$F_\theta = \mathcal{J}_1 (q - q_0)^2 - \frac{D_{sc}^2}{4\mathcal{J}_1} = \frac{K_c}{2} \left(\frac{q - q_0}{q_0}\right)^2 - \frac{D_{sc}^2}{4\mathcal{J}_1},$$

where the compression modulus K_c is given by

$$\boxed{K_c = 2\mathcal{J}_1 q_0^2 = \frac{D_{sc}^2}{2\mathcal{J}_1}.} \tag{11}$$

The pure in-plane splay and bend deformations do not involve the change of wave-vector amplitude but rather rotations of the propagation vector direction $\mathbf{e_q}$. Fixing $\mathbf{e}_z \parallel \mathbf{e_P}$ and $q = q_0$, Eq. (9) becomes

$$F_\theta = \text{const} + \frac{\mathcal{J}_1}{2} \|\boldsymbol{\nabla} \mathbf{e}_q\|_F^2 + 3\frac{\mathcal{J}_2}{2} |\partial_P \mathbf{e_q}|^2, \tag{12}$$

and, using Frank decomposition for a twist-free case without boundary contributions

$$\|\boldsymbol{\nabla} \mathbf{v}\|_F^2 = (\boldsymbol{\nabla} \cdot \mathbf{v})^2 + |\mathbf{v} \times (\boldsymbol{\nabla} \times \mathbf{v})|^2,$$

we obtain

$$F_\theta = \text{const} + \frac{\mathcal{J}_1}{2} (S^2 + |\mathbf{B}|^2) + 3\frac{\mathcal{J}_2}{2} |\partial_P \mathbf{e_q}|^2, \tag{13}$$

where $S = \boldsymbol{\nabla} \cdot \mathbf{e_q}$ and

$$\mathbf{B} = -(\mathbf{e_q} \cdot \nabla)\mathbf{e_q} = \mathbf{e_q} \times (\boldsymbol{\nabla} \times \mathbf{e_q}) \tag{14}$$

Coefficient	Microscopic expression	Value [meV,Å]	[erg,cm]
A	$(-3J_1+6J_2)/a_0^3$	1.78	2.85×10^{9}
$\mathcal{J}_1$	$(-J_1+4J_2-\Delta J_2)/(2a_0)$	4.34	6.95×10^{-7}
$\mathcal{J}_2$	$\Delta J_2/(2a_0)$	0.15	0.24×10^{-7}
Λ	$-6J_1/a_0^3$	3.68	5.89×10^{9}
$\mathcal{D}_{sc}$	D_{sc}/a_0^2	0.049	0.787
$\mathcal{D}_w$	$3D_w/a_0^3$	0.022	3.54×10^{7}
$\mathcal{K}$	K/a_0^3	6×10^{-4}	9.5×10^{5}

Table 1: Correspondence between microscopic Hamiltonian parameters and continuum coefficients.

denote the splay and $\mathbf{e_q}$ bend vector, respectively. The first two terms in Eq.(13) correspond to isotropic in-plane bend/splay elasticity with equal bend and splay moduli

$$\boxed{K_s = K_b = \mathcal{J}_1}. \tag{15}$$

The last term has a meaning of an additional oerientational stiffness penalizing inhomogneoeus bend/splay variations along the polar vector $\mathbf{e_P}$. We note that, in the main text we have used the symbol Γ to denote splay and bend moduli.

Auxiliary expressions

The energy functional in the continuum limit is obtained by setting $\mathbf{r}_j = \mathbf{r}_i + \boldsymbol{\tau}_{ij}$ where $\boldsymbol{\tau}_{ij}$ denotes the bond vector and expanding the slow variables $\mathbf{n}$ and $\mathbf{m}$ in powers of the lattice derivative $D = \boldsymbol{\tau}_{ij}\cdot\boldsymbol{\nabla}$

$$\mathbf{n}_j = \mathbf{n}_i + D\,\mathbf{n}_i + \frac{1}{2}D^2\,\mathbf{n}_i + O(D^3), \tag{16}$$

$$\mathbf{m}_j = \mathbf{m}_i + D\,\mathbf{m}_i + \frac{1}{2}D^2\mathbf{m}_i + O(D^3). \tag{17}$$

First, we obtain approximate expressions for the following terms appearing in Eq.(1)

$$s_i^\alpha s_j^\beta = \eta_i\eta_j\gamma_i\gamma_j\, n_i^\alpha n_j^\beta + \eta_i\gamma_i\, n_i^\alpha m_j^\beta + \eta_j\gamma_j\, m_i^\alpha n_j^\beta + m_i^\alpha m_j^\beta, \tag{18}$$

$$\mathbf{s}_i\times\mathbf{s}_j = \eta_i\eta_j\gamma_i\gamma_j\,\mathbf{n}_i\times\mathbf{n}_j + \eta_i\gamma_i\,\mathbf{n}_i\times\mathbf{m}_j + \eta_j\gamma_j\,\mathbf{m}_i\times\mathbf{n}_j + \mathbf{m}_i\times\mathbf{m}_j \tag{19}$$

Using Eqs.(16-17) and assuming the weak magnetization amplitude is of the order of magnitude of D ($m^\alpha \sim O(D)$) gives

$$\begin{aligned} s_i^\alpha s_j^\beta =& \eta_{ij}\gamma_{ij}(n^\alpha n^\beta + n^\alpha Dn^\beta + \frac{1}{2}n^\alpha D^2 n^\beta) + \\ &+ \eta_i(n^\alpha m^\beta + n^\alpha Dm^\beta) + \eta_j(m^\alpha n^\beta + m^\alpha Dn^\beta) + \\ &+ m^\alpha m^\beta + O(D^3), \end{aligned} \tag{20}$$

and

$$\begin{aligned} \mathbf{s}_i \times \mathbf{s}_j =& \eta_{ij}\gamma_{ij}(\mathbf{n} \times D\mathbf{n} + \frac{1}{2}\mathbf{n} \times D^2\mathbf{n}) + \\ &+ \eta_i(\mathbf{n} \times \mathbf{m} + \mathbf{n} \times D\mathbf{m}) + \eta_j(\mathbf{m} \times \mathbf{n} + \mathbf{m} \times D\mathbf{n}) \\ &+ O(D^3), \end{aligned} \tag{21}$$

where $\eta_{ij} = \eta_i\,\eta_j$, $\gamma_{ij} = \gamma_i\gamma_j \approx (1 - m^2)$ and all right hand side expressions are evaluated at $\mathbf{r}_i$. After explicitly separating the full derivatives

$$\begin{aligned} &\frac{1}{2}n^\alpha D^2 n^\beta = \frac{1}{2}D(n^\alpha Dn^\beta) - \frac{1}{2}Dn^\alpha Dn^\beta, \\ &\frac{1}{2}\mathbf{n} \times D^2\mathbf{n} = \frac{1}{2}D(\mathbf{n} \times D\mathbf{n}), \end{aligned} \tag{22}$$

and some simplifications we obtain

$$\begin{aligned} s_i^\alpha s_j^\beta \approx& \Big[\eta_{ij}(1 - m^2)n^\alpha n^\beta + \eta_{ij}(n^\alpha Dn^\beta - \frac{1}{2}Dn^\alpha Dn^\beta) + \\ &+ \eta_i(n^\alpha m^\beta + n^\alpha Dm^\beta) + \eta_j(m^\alpha n^\beta + m^\alpha Dn^\beta) + \\ &+ m^\alpha m^\beta\Big] + \frac{\eta_{ij}}{2}D(n^\alpha Dn^\beta), \\ \mathbf{s}_i \times \mathbf{s}_j \approx& [\eta_{ij}\mathbf{n} \times D\mathbf{n} + (\eta_i - \eta_j)\mathbf{n} \times \mathbf{m} + (\eta_i + \eta_j)\mathbf{n} \times D\mathbf{m}] + \\ &+ \eta_j D(\mathbf{m} \times \mathbf{n}) + \frac{\eta_{ij}}{2}D(\mathbf{n} \times D\mathbf{n}) + O(D^3). \end{aligned} \tag{23}$$

In our case, the boundary terms (outside of square brackets) will be omitted from the energy functional. Furthermore, exchange contributions linear in D cancel after summing over j since symmetric exchange $J_{ij}^{\alpha\beta} = J_\tau^{\alpha\beta} = J_{-\tau}^{\alpha\beta}$ while $D = \boldsymbol{\tau}_{ij} \cdot \boldsymbol{\nabla}$ changes sign. Therefore,

$$-\frac{1}{2}\sum_{ij} J_{ij}^{\alpha\beta} s_i^\alpha s_j^\beta \approx \int d^3r \left[\mathcal{J}_{\alpha\beta}^{\gamma\delta}(\partial_\gamma n^\alpha)(\partial_\delta n^\beta) - (1 - m^2)A_{\alpha\beta}n^\alpha n^\beta - B_{\alpha\beta}m^\alpha m^\beta\right], \tag{24}$$

where $\mathcal{J}$ is the exchange stiffness tensor

$$\mathcal{J}_{\alpha\beta}^{\gamma\delta} = \frac{1}{4a_0^3}\sum_\tau J_\tau^{\alpha\beta}\eta_\tau\tau_\gamma\tau_\delta = \frac{\delta^{\gamma\delta}}{2a_0}\left(-J_1^{\alpha\beta} + 3J_{2,1}^{\alpha\beta} + J_{2,2}^{\alpha\beta}\right) + 3\frac{e_P^\gamma e_P^\delta}{2a_0}(J_{2,2}^{\alpha\beta} - J_{2,1}^{\alpha\beta}), \tag{25}$$

where J_1 is the first nearest neighbors exchange tensor, while $J_{2,1}$ and $J_{2,2}$ denote the next nearest neighbor constants for the two $R3c$ classes of second nearest neighbor bonds. Specifically, $J_{2,1}$ describes the exchange for six bonds perpendicular to $\mathbf{e_P}$ while $J_{2,2}$ corresponds to bonds with non-zero $\mathbf{e_P}$ projection. The expression can be further simplified by separating the diagonal $\gamma = \delta$ part of the $\mathcal{J}^{\gamma\delta}_{\alpha\beta}$ tensor. For this, we use $e^{\gamma}_P e^{\delta}_P = \delta^{\gamma\delta}/3 + (1-\delta^{\gamma\delta})e^{\gamma}_P e^{\delta}_P$ to obtain

$$\mathcal{J}^{\gamma\delta}_{\alpha\beta} = \frac{\delta^{\gamma\delta}}{2a_0}\left(-J_1^{\alpha\beta} + 4\frac{J_{2,1}^{\alpha\beta}+J_{2,2}^{\alpha\beta}}{2}\right) + 3\frac{1-\delta^{\gamma\delta}}{2a_0}(J_{2,2}^{\alpha\beta}-J_{2,1}^{\alpha\beta})e^{\gamma}_P e^{\delta}_P, \tag{26}$$

where $\delta^{\gamma\delta} = \delta_{\gamma\delta}$ denotes the Kronecker delta symbol. Introducing the average second nearest neighbor exchange $J_2^{\alpha\beta} = (J_{2,1}^{\alpha\beta} + J_{2,2}^{\alpha\beta})/2$ and the difference $\Delta J_2 = J_{2,2}^{\alpha\beta} - J_{2,1}^{\alpha\beta}$ we finally obtain

$$\mathcal{J}^{\gamma\delta}_{\alpha\beta} = \frac{-J_1^{\alpha\beta} + 4J_2^{\alpha\beta}}{2a_0}\delta^{\gamma\delta} + 3\left(1-\delta^{\gamma\delta}\right)\frac{\Delta J_2^{\alpha\beta}}{2a_0}e^{\gamma}_P e^{\delta}_P, \tag{27}$$

The $A_{\alpha,\beta}$ and $B_{\alpha\beta}$ coefficients are given by

$$\begin{aligned} A_{\alpha\beta} &= \frac{1}{2a_0^3}\sum_{\tau} J_{\tau}^{\alpha\beta}\eta_{\tau} = \frac{1}{a_0^3}\left(-3J_1^{\alpha\beta} + 6J_2^{\alpha\beta}\right), \\ B_{\alpha\beta} &= \frac{1}{2a_0^3}\sum_{\tau} J_{\tau}^{\alpha\beta} = \frac{1}{a_0^3}\left(3J_1^{\alpha\beta} + 6J_2^{\alpha\beta}\right), \end{aligned} \tag{28}$$

characterize the local exchange energies of the Néel and weak-magnetization sectors, respectively. In the presence of exchange anisotropy, they act as effective anisotropy tensors. Assuming that the exchange tensors are diagonal, these expressions further simplify resulting in the exchange stiffness expression given in Eq.(4).

The evaluation of the cross product sum following from Eq.(23) is slightly different. First, we represent the DMI vector as a sum of spin current (D_{sc}) and weak-ferromagnetic/staggered (D_w) terms $\mathbf{D}_{ij} = D_{sc}(\boldsymbol{\tau}\times\mathbf{e}_P)/\tau + (\eta_i - \eta_j)D_w\mathbf{e}_P/2$. Then, from Eq.(23), the nearest neighbor staggered contribution can be approximated as

$$\frac{D_w}{4}\sum_{ij}(\eta_i-\eta_j)\mathbf{e}_P[\mathbf{s}_i\times\mathbf{s}_j] \approx \int d^3r\frac{3D_w}{a_0^3}\mathbf{e}_P\cdot[\mathbf{n}\times\mathbf{m}], \tag{29}$$

where we have omitted the boundary contributions and the fast oscillating term $\eta_i\mathbf{n}\times D\mathbf{n}$. Applying the same logic to the nearest neighbor spin current DMI sum, we obtain the Lifshitz invariant

$$\frac{D_{sc}}{2}\sum_{ij}\frac{1}{\tau}(\boldsymbol{\tau}\times\mathbf{e}_P)[\mathbf{s}_i\times\mathbf{s}_j] \approx \int d^3r\frac{-D_{sc}}{a_0^2}\left[\mathbf{e}_P\cdot(\mathbf{n}\cdot\boldsymbol{\nabla})\,\mathbf{n} - (\mathbf{n}\cdot\mathbf{e}_P)(\boldsymbol{\nabla}\cdot\mathbf{n})\right], \tag{30}$$

Finally, the anisotropy term, assuming $\mathbf{m}\perp\mathbf{e}_P$, is equal to

$$K\sum_i(\mathbf{s}_i\cdot\mathbf{e}_P)^2 \approx \int d^3r\frac{K}{a_0^3}(1-m^2)(\mathbf{n}\cdot\mathbf{e}_P)^2, \tag{31}$$

where the m^2 correction is usually omitted since the anisotropy constant $\mathcal{K}$ is much smaller than the exchange and DMI contributions.

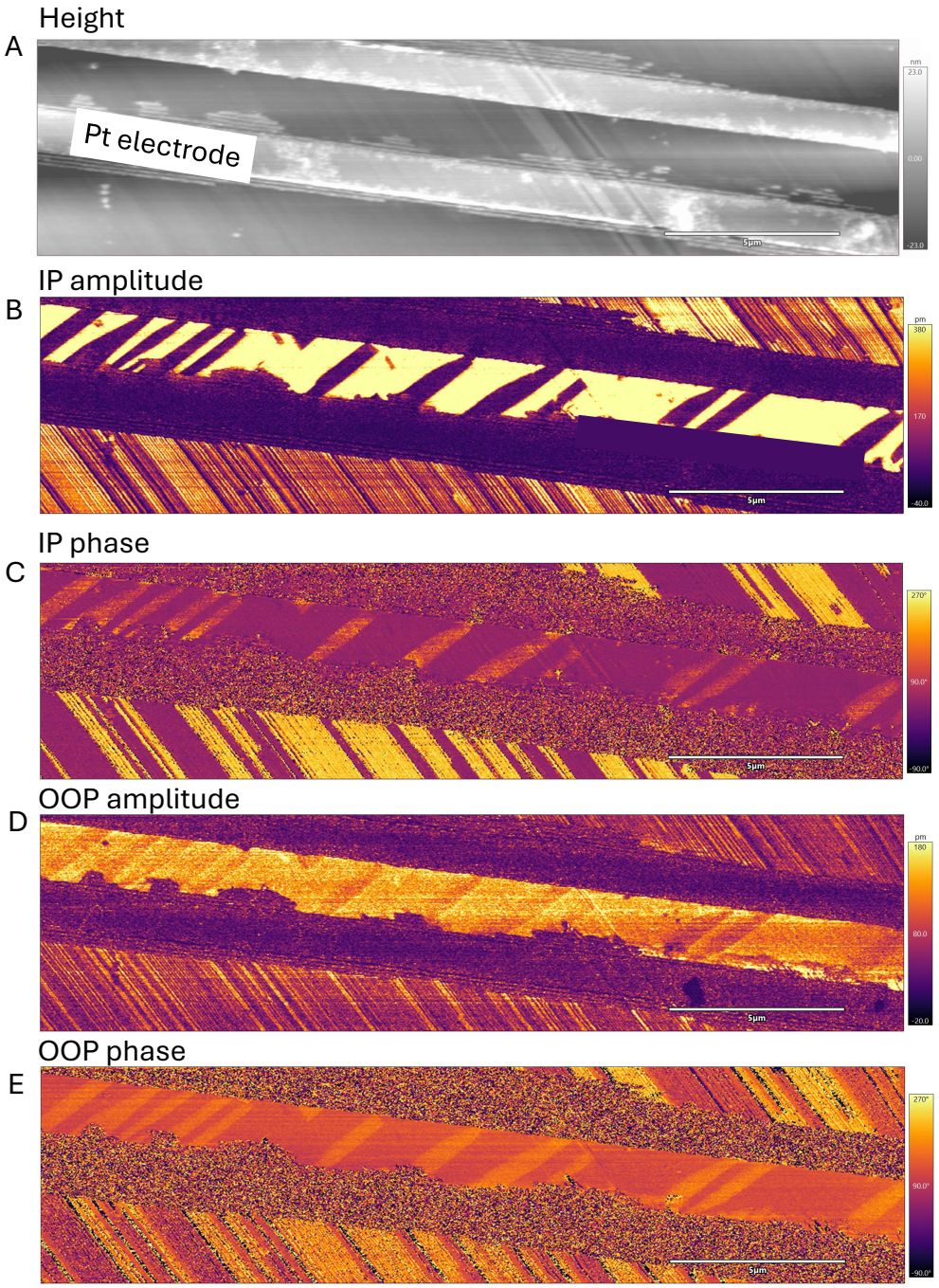

Fig. S 1: **Reproducibility of large poled 71° ferroelectric monodomains at different locations.** (A) Topographic image of the in-plane platinum electrodes used to pole the sample and generate large ferroelectric domains. The electrode spacing was typically 1–2 μm, and the electrodes were oriented at 45° with respect to the as-grown 109° ferroelectric domains. (B,C) In-plane piezoresponse force microscopy (PFM) amplitude and phase images, respectively, showing the formation of large 71° ferroelectric domains spanning several microns in the region between the electrodes. (D,E) Out-of-plane piezoresponse force microscopy (PFM) amplitude and phase images, shown in panels D and E, respectively. The slight contrast in the out-of-plane channel is primarily attributed to crosstalk.

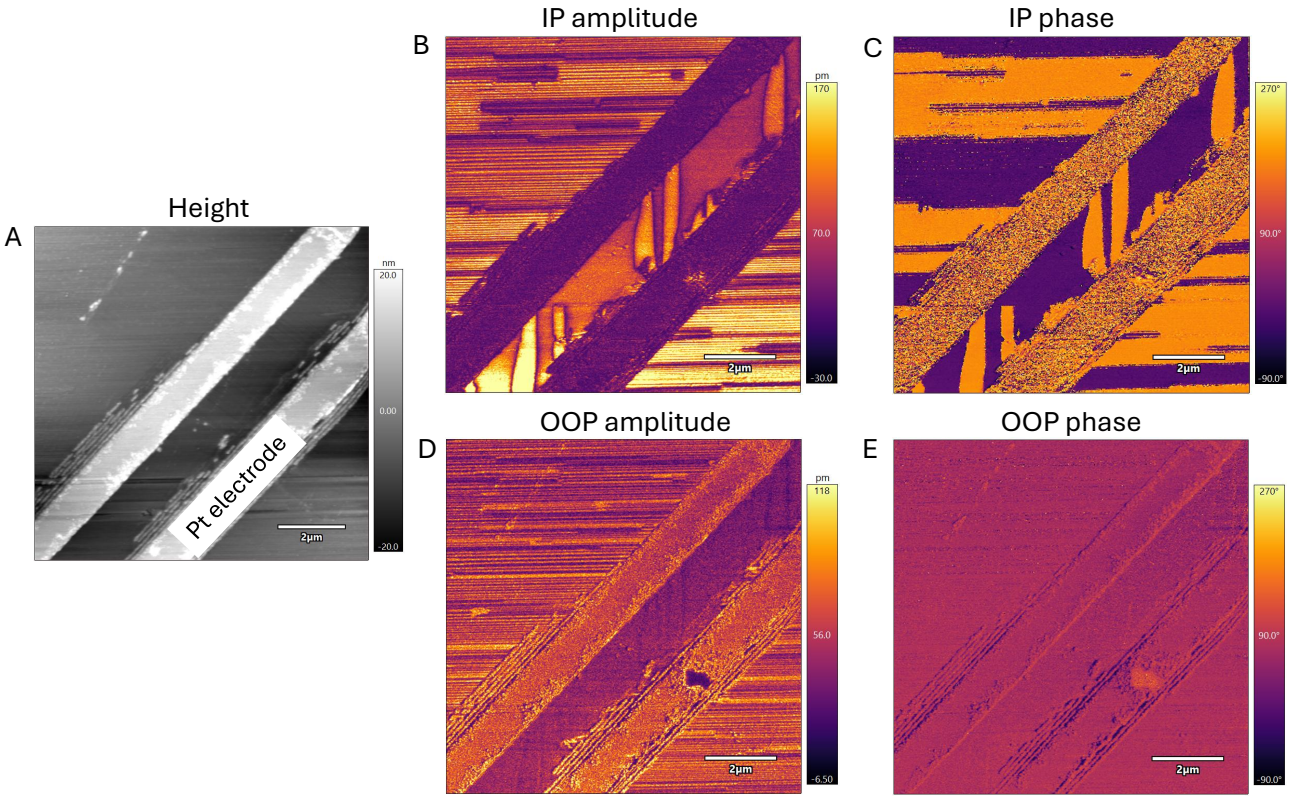

Fig. S 2: **PFM imaging after rotating the sample by 45°.** (A) Topographic image of the in-plane platinum electrodes used to pole the sample and generate large ferroelectric domains. (B,C) In-plane PFM amplitude and phase images, respectively, revealing the formation of large 71° ferroelectric domains. (D,E) Out-of-plane PFM amplitude and phase images, shown in panels D and E, respectively. The lack of significant contrast in the out-of-plane channel between the electrodes is consistent with the formation of 71° domains.

Supplementary note S2. How does ferroelectric domain walls determine the propagation vector of a spin cycloid in $BiFeO_3$?

In Fig. 2 of the main text and Extended data Figs. 4-6, we presented detailed SNVM imaging to demonstrate how ferroelectric domain walls pin the spin cycloid propagation vector. This pinning is manifested by the gradual loss of cycloid director alignment beyond a critical distance from the domain wall. Remarkably, we found that the cycloid propagation direction near an electrically nucleated 71° ferroelectric domain wall in $BiFeO_3$ grown on $TbScO_3$ is identical to that observed near a 71° ferroelectric domain wall (which is as grown state) in $BiFeO_3$ grown on $DyScO_3$ (Extended data Fig. 7). These observations provide strong evidence that the ferroelectric domain walls themselves play a pivotal role in lifting the threefold bulk degeneracy of the cycloid propagation vector, contrary to the commonly held view that this selection is primarily dictated by anisotropic strain imposed by the substrate (*1–3*). Such behavior is not entirely unexpected. Previous theoretical studies have examined which cycloid propagation vectors are energetically compatible across ferroelectric domain walls and have predicted a variety of possible configurations without explicitly invoking substrate-induced strain (*4*).

Motivated by these considerations, we carried out simulations of spin cycloids across a 71° domain wall (Supplementary Fig. S3). A series of representative snapshots illustrating the evolution of the spin texture are shown in Fig. S3. For this we have used the effective Hamiltonian model (***?***) that parameterizes both the structural and magnetic energy landscapes of $BiFeO_3$ obtained from density functional theory simulations. To allow for a maximum freedom for system to chose the cycloidal propagation vectors and phases in both domains, the relaxation was carried in two steps. First, the structural and spin relaxations were carried out at T=800K which is above the magnetic N'eel temperature but below the ferroelectric Curie temperature of $BiFeO_3$. The initial state for this relaxation was chosen to correspond to a single 71° ferroelectric domain wall within the 80x80x16 supercell. The direction of polarization within the described domain structure is shown in the left panel of Fig. S3. After a 100ps molecular and spin dynamics relaxation, we found that the ferroelectric domain wall structure was stable and sufficiently relaxed to proceed to the second relaxation stage. Here, the system state relaxed at 800K was subjected to an abrupt temperature quench mimicked by a direct relaxation at room tomperture without any temperature annelaing. Such temperature quench was performed to allow the system to spontaneously chose a preferred cycloid propagation directions within both of the ferroelectric domains while, at the same time, maximising the chances of magnetic defect formation (***?***). The described two-stage quench relaxation was then performed 50 times with distinct random seeds resulting in different magnetic structures at 71° domain walls. Several representative cycloidal states obtained from these simulations are depicted in Fig. S3.

While in Fig. S3 one can see formation of dislocations in the vicinity of the ferroelectric domain wall, we found that all independent quenches resulted in the same cycloidal propagation vectors within both ferroelectric domains. Namely, in the [111] polar domain, we found that the relaxed cycloid patterns featured a $[1\bar{1}0]_{\text{p.c.}}$ wave-vector while the $[1\bar{1}1]$ domain was characterized by the [110] propagation vector. This result evidences the domain wall induced confinement of cycloid propagation directions.

A microscopic driver of such confinement can be traced back to the spin exchange interaction requiring the least possible deformation of the cycloidal pattern across the domain wall. The corresponding conditions can be split into two separate criteria. The first one is related to the continuity of the spin rotation plane across the domain wall. Here, a perfect matching cannot be strictly satisfied, but the minimization of the corresponding exchange gradients can lead to the pinning of the cycloid phase shift across the domain wall.

The second condition is more strict and pertains to the matching of cycloid phase gradients at the domain wall. To avoid large compression deformations extending over the full wall area, the cycloid period as well as layer normals within the domain wall plane should match, thereby requiring the matching of the cycloid wave-vector projections on the domain wall. This matching condition can be thus expressed as continuity of the wave-vector projection on the wall plane. Equivalently,

$$\mathbf{q}_1 - \mathbf{q}_2 \parallel \mathbf{n}, \tag{32}$$

where $\mathbf{q}_1$ and $\mathbf{q}_2$ denote the cycloid wave-vectors in the two adjacent ferroelectric domains while $\mathbf{n}$ stands for the domain wall normal. This condition can significantly constrain the rotational symmetry of the cycloid propagation vectors, particularly in the presence of ferroelestic domain walls. To see this, we first consider charge neutral and mechanically compatible walls. For rhombohedral polarization directions, such ideal walls satisfy

$$\mathbf{P}_1 + \mathbf{P}_2 \parallel \mathbf{n} \tag{33}$$

and/or

$$(\mathbf{P_1} - \mathbf{P_2}).\mathbf{n} = 0 \tag{34}$$

where $\mathbf{P}_1$ and $\mathbf{P}_2$ denote the polarization vectors in adjacent domains. From Eq. (33), we find that any $\mathbf{q}_1 \perp \mathbf{P}_1$ will have a single matching $\mathbf{q}_2 \perp \mathbf{P}_2$ counterpart satisfying the continuity condition given by Eq. (32). At the same time, it is At the same time, in the case of a ferroelastic wall failing Eq.(33), only a few wave-vector directions will allow to satisfy the continuity condition Eq. (32). For instance, a 71° wall between $\mathbf{P}_1 \parallel [111]_{\text{p.c.}}$ and $\mathbf{P}_2 \parallel [1\bar{1}1]_{\text{p.c.}}$ oriented perpendicular to $\mathbf{n} = [100]_{\text{p.c.}}$ the possible $\mathbf{q}_1$ and $\mathbf{q}_2$ wave-vectors are

$$\mathbf{q}_1 \parallel [\bar{1}10]_{\text{p.c.}},\ \mathbf{q}_2 \parallel [110]_{\text{p.c.}} \tag{35}$$

or

$$\mathbf{q}_1 = \mathbf{q}_2 \parallel [101]_{\text{p.c.}}. \tag{36}$$

Therefore, we can conclude that 1) for mechanically compatible domain walls, there is a one-to-one correspondence between orientations of the cycloid wave-vector in the adjacent domains and 2) ferroelestic domain walls break the continuous rotational symmetry of the cycloid propagation directions. Finally, it is worth noting that for any wall, there exist two special directions $\pm\mathbf{P}_1 \times \mathbf{P}_2$ allowing for a seemless matching of propagation vectors.

On experimental front, achieving a microscopic understanding of this pinning mechanism requires direct structural information in the vicinity of the domain wall, ideally through cross-sectional transmission electron microscopy. However, obtaining such information for 71° walls is experimentally

challenging because of their geometry (*5*). To gain insight into the relevant structural factors that need to be considered near a ferroelectric domain wall, we performed 4D-STEM nanobeam diffraction and reconstructed maps of the in-plane strain (ε_{xx}), out-of-plane strain (ε_{yy}), lattice rotation, and shear strain (ε_{xy}) across a 109° ferroelectric domain wall, which offers a favorable front-on geometry. The resulting maps are summarized in Supplementary Fig. S4. As evident from these measurements, the strain fields near the domain wall are highly inhomogeneous. In particular, the in-plane and out-of-plane strain components are generally unequal and, in many regions, even exhibit changes in sign across the wall. In addition, the shear strain maps reveal a pronounced contrast associated with the domain boundary. These local variations may provide a microscopic basis for the emergence of the different cycloid configurations (Type I, Type II, and related variants) observed in the as-grown state. Taken together, these results suggest that the microscopic pinning of the cycloid director by ferroelectric domain walls is likely governed by a complex interplay of local strain gradients, shear distortions, and structural compatibility conditions. More broadly, these observations indicate that a complete microscopic understanding of cycloid director pinning requires going beyond homogeneous substrate-induced strain and accounting for the complex local structural environment at the domain wall. Elucidating this interplay between lattice distortions and magnetic order remains an important direction for future investigations.

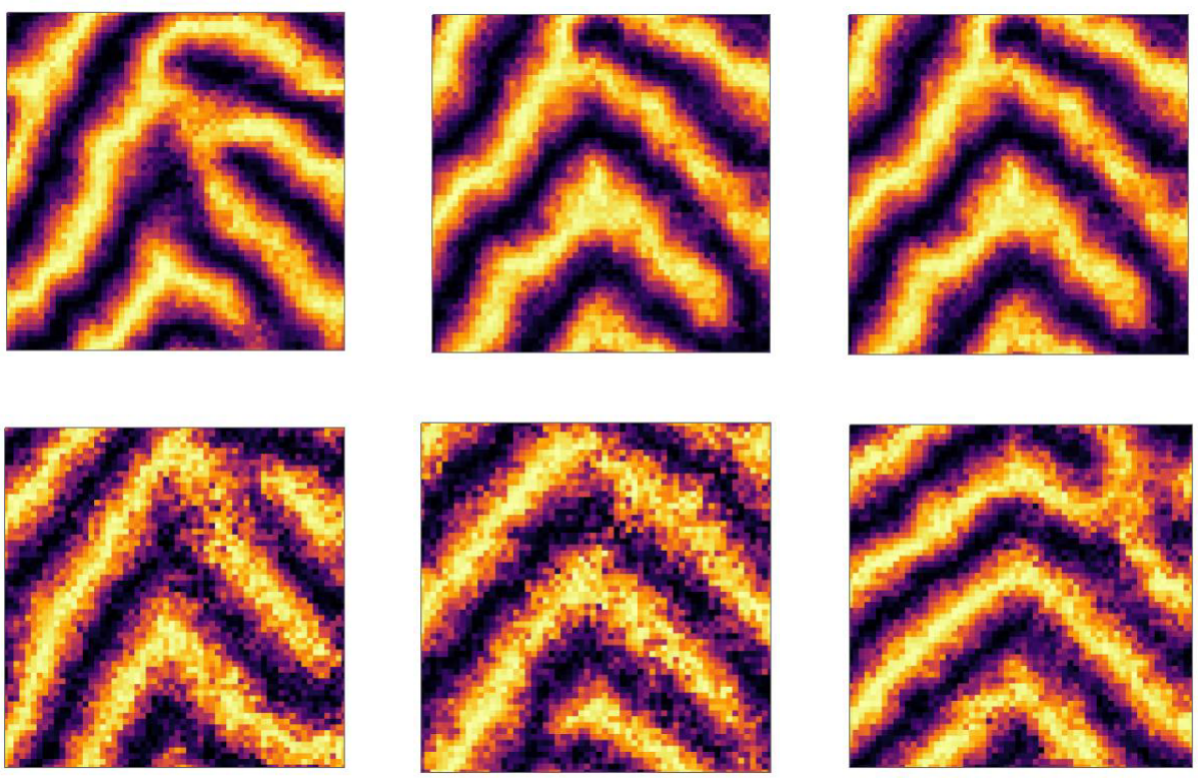

Fig. S 3: Simulated cycloidal structure of the 71° ferroelectric domain wall. The 80x80x16 supercell is divided into two ferroelectric domains along the horizontal $[100]_{\text{p.c.}}$ axis with polarizations oriented along $[111]_{\text{p.c.}}$ and $[1\bar{1}1]_{\text{p.c.}}$ crystolagraphic axes, respectively. A schematic representation of the simulated domain wall state is depicted in the left panel. Six panels on the right show simulated projection of the Néel vector on the polarization direction within the $(001)_{\text{p.c.}}$ supercell plane. Different panels correspond to results of distinct temperature quench relaxations of spins with different random seeds.

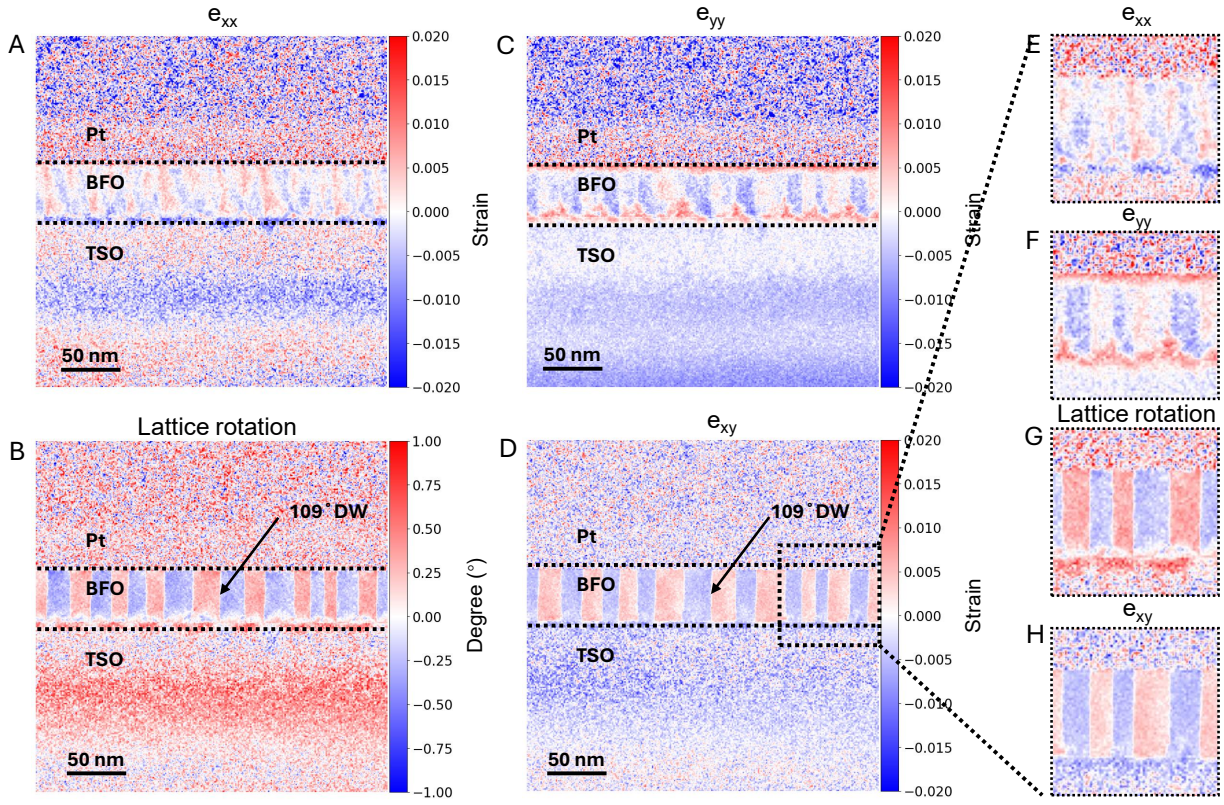

Fig. S 4: **Strain mapping of 109° ferroelectric–ferroelastic domains using 4D-STEM nanobeam diffraction.** (A–D) Maps of the in-plane strain e_{xx} (A), out-of-plane strain e_{yy} (B), lattice rotation (C), and shear strain e_{xy} (D). (E–H) Magnified views of the corresponding strain maps highlighting the local strain distribution across the $BiFeO_3$ (BFO) 109° ferroelectric–ferroelastic domains.

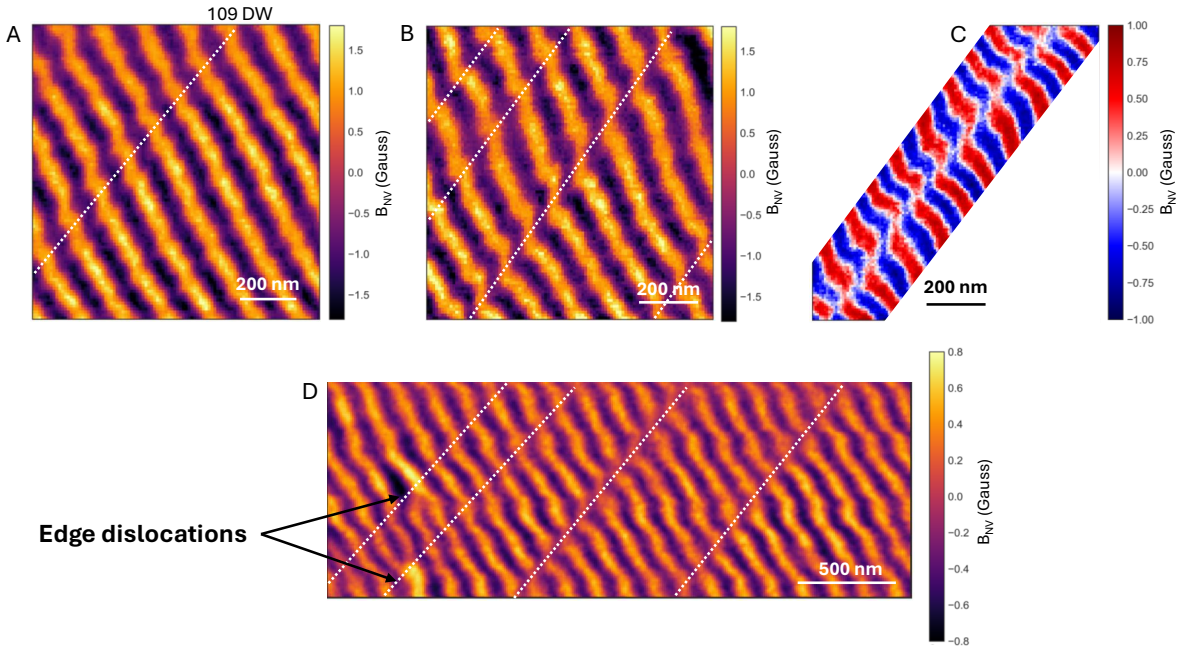

Fig. S 5: **Additional results on the observation of kinks at 109° domain walls. (A,B)** SNVM images of 109° domain walls, indicated by dotted white lines, showing clear kinks consistent with twisting of the smectic layer, as discussed in the main text. **(C)** Cropped section of a kink structure, highlighting the constriction of the cycloid near the domain wall. **(D)** Formation of an edge dislocation near the domain wall in a 100 nm-thick film on a $TbScO_3(110)_o$ substrate.

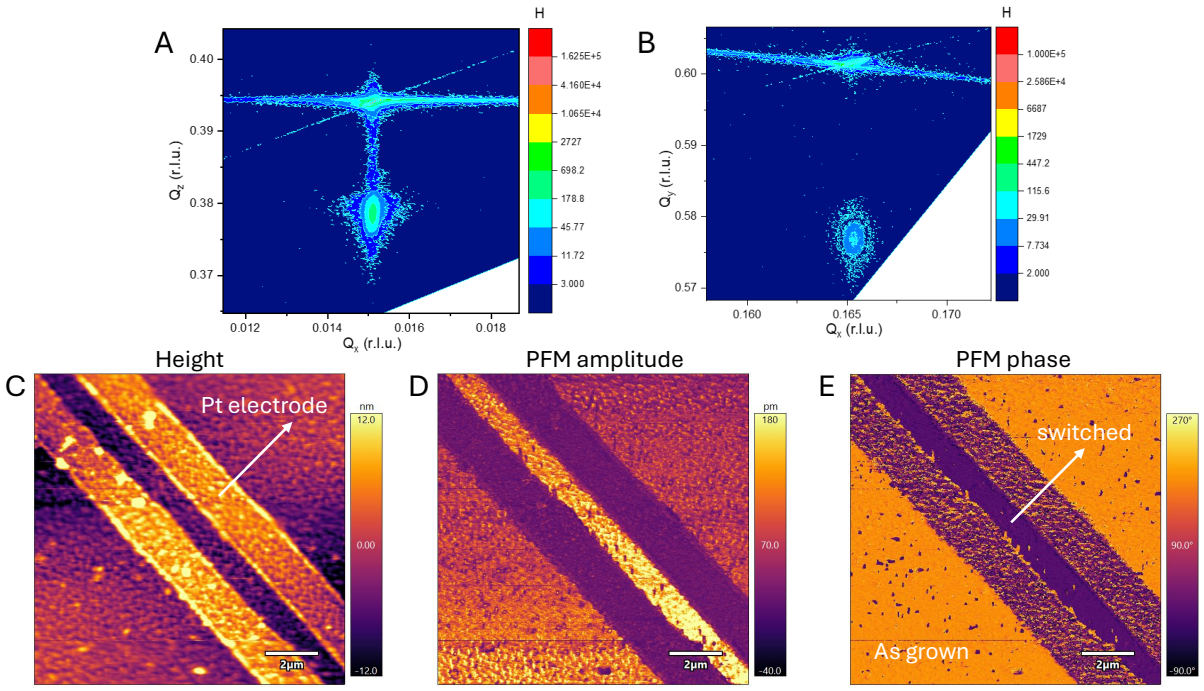

Fig. S 6: Structural characterization of a 15 nm $BiFeO_3$ film grown on a 4° vicinal $SrTiO_3$ substrate. (A,B) Reciprocal space maps around the (002) and (103) diffraction peaks (pseudocubic notation), demonstrating stabilization of a single ferroelastic domain. (C) Topography image of in-plane platinum electrodes used for poling. (D,E) In-plane PFM amplitude and phase images. Regions outside the electrodes show predominantly single-phase contrast with some minor domains (likely due to topography) in the as grown state. Upon electric field switching, the phase between the electrodes reverses by 180° and remains homogeneous over the entire electrode region signifying retention of ferroelectric mono domain even after an electric field switching.

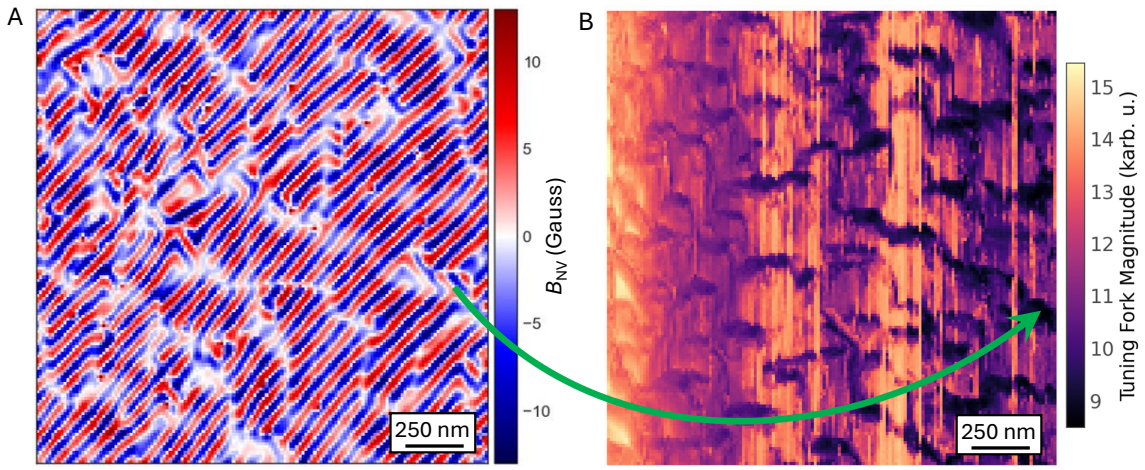

Fig. S 7: Origin of discontinuities in cycloids observed in a 15 nm $BiFeO_3$ film on vicinal $SrTiO_3$(001) substrate. (A) Full-B SNVM image of the magnetic contrast, displayed using a seismic color scale. This is the same image as shown in Fig. 4 of the main text. (B) Tuning-fork magnitude channel recorded simultaneously during the SNVM scan, showing that the cycloid lattice discontinuities can be attributed to imperfections in the substrate terraces.

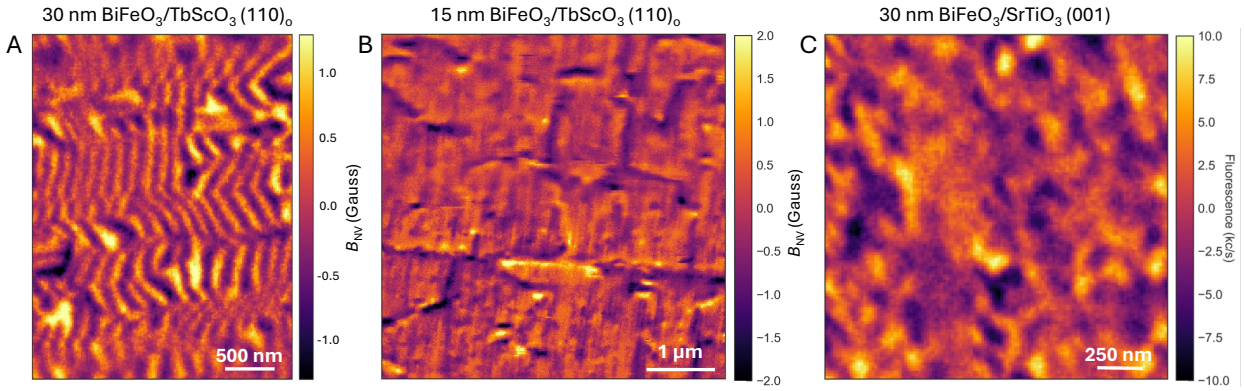

Fig. S 8: **NV images of thinner $BiFeO_3$ films on $TbScO_3(110)_o$ and flat $SrTiO_3(001)$ substrates.** (A) NV image of a 30 nm $BiFeO_3$ film on $TbScO_3(110)_o$, showing frustrated cycloids with random propagation vectors even within well-defined ferroelectric domains, indicating instability. (B) Upon further reduction of film thickness to 15 nm, cycloids vanish completely. Interestingly, for films grown on flat $SrTiO_3$, cycloids are not stable even at 30 nm thickness (panel C). Notably, all of these films lack a bottom electrode.

Supplementary note 3. Magnon transport induced by Spin Seebeck

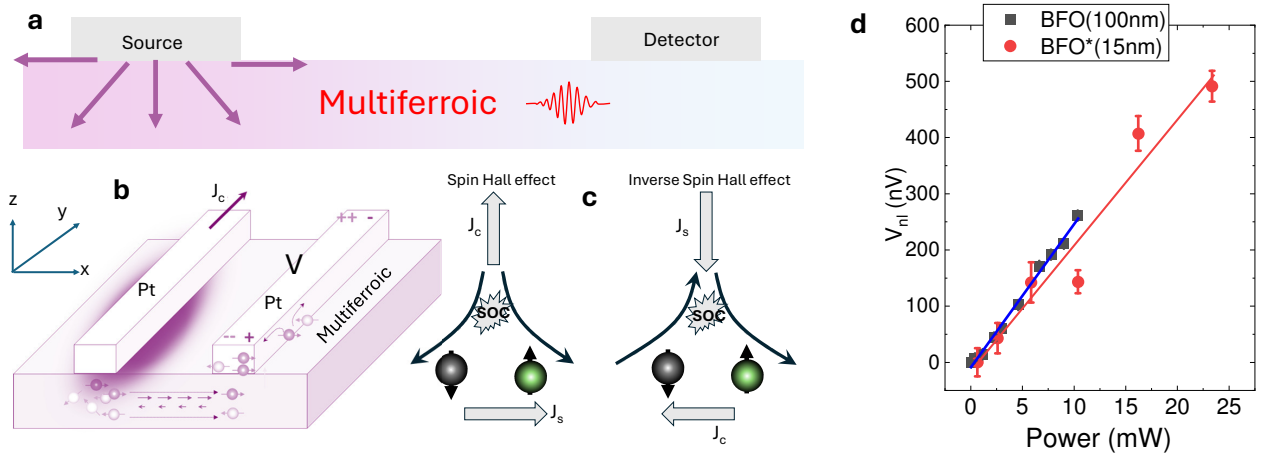

Fig. S 9: Heating power dependent magnon transport in BFO(100nm) deposited on TSO and BFO(15nm) on 4°miscut STO substrate. * Represents the BFO with a featured substrate having a 4-degree miscut. The lines are the linear fit, suggesting spin-Seebeck-effect-driven magnon transport in BFO thin films.

In our experimental geometry, magnons in the multiferroic insulator are thermally excited using a Pt injector. Our primary objective is to investigate thermally generated magnons to gain insight into single-domain multiferroic physics and its influence on magnon transport. For this purpose, we focus on the second-harmonic nonlocal response, which originates from thermally driven spin currents. A charge current applied to the Pt injector generates Joule heating, resulting in a radial heat distribution around the injector wire (Supplementary Figure S9a). The resulting temperature gradient, ∇T, across the magnetic insulator creates a spatial imbalance in the magnon population. Consequently, magnons diffuse from the hotter region toward the colder region, giving rise to the spin Seebeck effect (SSE). Although heat does not directly couple to magnons, the temperature gradient generates phonons that interact with magnons through magnon–phonon scattering. At finite temperatures, this interaction plays a crucial role in the generation, transport, and relaxation of thermally excited magnons. All measurements presented in this work are performed at room temperature, ensuring comparable phonon contributions across different measurement configurations. Magnon–phonon scattering contributes to the relaxation of magnon spin accumulation and is closely related to the effective Gilbert damping of the magnetic system. Importantly, thermally excited magnons are not confined to the immediate vicinity of the injector; instead, they propagate over several micrometers depending on the magnitude of the thermal gradient and the magnon diffusion length. Our analysis emphasizes a relative comparison of magnon transport properties between two BFO thin films prepared differently. On the detector side, the Pt strip should not be regarded merely as a passive heat sink. The thermal gradient estab-

lishes a magnon chemical potential gradient, characterized by magnon depletion beneath the injector and magnon accumulation beneath the detector. This gradient drives the transfer of magnon angular momentum into the detector region.

At the detector interface, the spin current carried by magnons is converted into an electrical voltage via the inverse spin Hall effect (ISHE) in Pt, enabled by its strong spin-orbit coupling (SOC), as illustrated in Supplementary Figure S9 b-c. Under open-circuit conditions, the injected spin current generates a transverse charge accumulation that can be measured as a voltage, as shown in Supplementary Figure S9 d.

References

1. P. Meisenheimer, G. Moore, S. Zhou, H. Zhang, X. Huang, S. Husain, X. Chen, L. W. Martin, K. A. Persson, S. Griffin, L. Caretta, P. Stevenson, R. Ramesh, *Nature Communications* **15**, 2903 (2024).

2. P. Meisenheimer, M. Ramesh, S. Husain, I. Harris, H. W. Park, S. Zhou, H. Taghinejad, H. Zhang, L. W. Martin, J. Analytis, *et al.*, *Advanced Materials* **36**, 2404639 (2024).

3. P. Pal, J. L. Schad, A. M. Vibhakar, S. K. Ojha, S. H. G.-Y. Kim, S. Shenoy, F. Xue, K. Das, Y. Kumar, P. Lenharth, *et al.*, *arXiv preprint arXiv:2410.22447* (2024).

4. F. Xue, T. Yang, L.-Q. Chen, *Physical Review B* **103**, 064202 (2021).

5. Y. Wang, C. Nelson, A. Melville, B. Winchester, S. Shang, Z.-K. Liu, D. G. Schlom, X. Pan, L.-Q. Chen, *Physical review letters* **110**, 267601 (2013).